

# PEO-*b*-PBD Diblock Copolymers Induce Packing Defects in Lipid/Hybrid Membranes and Improve Insertion Rates of Natively Folded Peptides

Jan Steinkühler, Miranda L. Jacobs, Margrethe A. Boyd, Citlayi G. Villaseñor, Sharon M. Loverde, and Neha P. Kamat\*



Cite This: *Biomacromolecules* 2022, 23, 4756–4765



Read Online

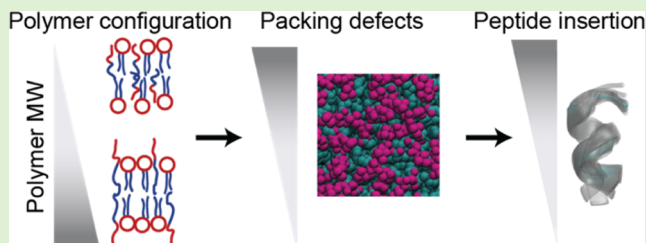
ACCESS |

Metrics & More

Article Recommendations

Supporting Information

**ABSTRACT:** Hybrid membranes assembled from biological lipids and synthetic polymers are a promising scaffold for the reconstitution and utilization of membrane proteins. Recent observations indicate that inclusion of small fractions of polymer in lipid membranes can improve protein folding and function, but the exact structural and physical changes a given polymer sequence imparts on a membrane often remain unclear. Here, we use all-atom molecular dynamics simulations to study the structure of hybrid membranes assembled from DOPC phospholipids and PEO-*b*-PBD diblock copolymers. We verified our computational model using new and existing experimental data and obtained a detailed picture of the polymer conformations in the lipid membrane that we can relate to changes in membrane elastic properties. We find that inclusion of low polymer fractions induces transient packing defects into the membrane. These packing defects act as insertion sites for two model peptides, and in this way, small amounts of polymer content in lipid membranes can lead to large increases in peptide insertion rates. Additionally, we report the peptide conformational space in both pure lipid and hybrid membranes. Both membranes support similar alpha helical peptide structures, exemplifying the biocompatibility of hybrid membranes.



## INTRODUCTION

Biological membranes are inherently heterogenous containing hundreds of distinct amphiphiles, and even relatively simple bacteria need at least a few different lipids to sustain life.<sup>1</sup> In addition to the many possible roles of lipid heterogeneity, this feature is increasingly thought to contribute to the successful folding and insertion of membrane proteins.<sup>2,3</sup> Model membranes have been useful to investigate the relationship between membrane composition and membrane protein folding and insertion. For example, lipid mixtures, compared to single component membranes, were found to increase protein yield in cell-free expression systems.<sup>2</sup> Assembling mixtures of charged and uncharged lipids improved the reinsertion and refolding of proteins upon force induced protein unfolding.<sup>3</sup> Further, increasing the number of lipid components in a membrane was found to inhibit protein misfolding and amyloid aggregation.<sup>4</sup> One reason that lipid composition may impact protein folding is because the lipids change the biophysical properties of the membrane and alter the energy required for a protein to insert and fold. Accordingly, previous studies have shown that protein folding and structure formation can be influenced by collective membrane properties such as elastic constraints of the membrane, charge–charge interactions, or membrane lateral pressure distribution.<sup>5–7</sup> To probe the role of membrane

properties on membrane protein folding and structure, it would be useful to access a wider range of membrane amphiphiles that expand the chemical and physical properties of bilayer membranes that are possible. This diversity would allow us to not only better probe the structure–function relationship of membranes and the proteins they hold but also design new types of membrane-based materials that bridge the advantages of both biological and synthetic components.

Toward this goal, a particularly interesting class of heterogenous model membranes are hybrid lipid/block-copolymer membranes. Hybrid membranes maintain biocompatibility with membrane proteins by including biological lipids and allow for carefully tailored physical and chemical properties provided by the polymers.<sup>8–13</sup> Additionally hybrid lipid/block copolymer membranes were shown before to often enhance membrane protein stability and functionality.<sup>14–16</sup> In previous works, membrane protein insertion is typically

Received: July 28, 2022

Revised: October 10, 2022

Published: November 1, 2022



induced by addition of membrane destabilizing detergents or divalent ions. Recently, we observed that the inclusion of a poly(ethylene oxide)-*b*-poly(butadiene) (PEO-*b*-PBD) diblock copolymer at 10–25 mol % in 1,2-dioleoyl-*sn*-glycerol-3-phosphocholine (DOPC) membranes increased the cell-free expression of two different transmembrane membrane proteins by a factor of up to 3, relative to pure phospholipid membranes without the addition of detergents.<sup>17</sup> Interestingly, the observed increases in the protein folding efficiency and yield depended not only on the total fraction of the polymer to phospholipid but also on the molecular weight (MW) of the polymer's chains, with low-MW polymer chains proving beneficial, while a higher-MW polymer inhibited cotranslational protein insertion. This study hinted at a systematic relationship between the polymer structure and membrane protein folding that we were interested in investigating further.

Molecular dynamics (MD) simulations have proven to be a useful approach to investigate structure–function relationships for polymer membranes.<sup>18–21</sup> In addition, MD simulations have successfully been used to systematically investigate amino acid and peptide partitioning free energies and kinetics with pure lipid bilayers.<sup>22–26</sup> Here, we employed MD simulations of heterogenous, hybrid, lipid/diblock copolymer membranes to gain more insight into the relationship between membrane physical features and membrane protein folding. As a first step in the protein folding process, we focused on short alpha helical peptides, which serve as a model of the nascent peptide chain, and investigated how these peptides adsorb and insert into hybrid membranes as a function of the lipid/polymer ratio.

This paper is divided into three parts: First, we parametrize PEO-*b*-PBD diblock copolymers and validate and compare our MDs model to experimental results. Second, we identify an unexpected configuration of low-MW polymer chains in hybrid membranes. Finally, we investigate the effects of membrane composition and structure on the insertion rates of two model peptides.

## MATERIALS AND METHODS

**MD Simulations. Simulation Setup and Parametrization.** A (1,2)-butadiene trimer was parametrized using CGenFF web server which parametrizes small molecules by analogy to established parametrizations for other molecules (<https://cgenff.umaryland.edu/>) for the CHARMM36 force field.<sup>48,49</sup> The quality of the analogy is measured by penalty scores which were always below 10 and indicate good agreement (*Supporting Information* Text 1). From the central repeat unit of the trimer, the 1,2 PB polymer (PBD) was assembled (Figure S4). To patch the PEO polymer (CHARMM36) to PBD, a linking carbon atom was again parametrized using CGenFF. Polymers were capped by a –OH group. PEO-*b*-PBD polymers were assembled using VMD (1.9.3)<sup>50</sup> and scripts.<sup>51</sup>

DOPC and DOPC + 10 mol % C12E8 bilayers were assembled using CHARMM-GUI with 150 amphiphiles per leaflet and initially equilibrated using the standard six-step CHARMM-GUI procedure and CHARMM36 force field.<sup>52,53</sup>

For lipid/polymer blends, the corresponding number of DOPC molecules were removed from a fully equilibrated bilayer and replaced with PEO-*b*-PBD molecules. Here, PEO-*b*-PBD was initially in a stretched linear conformation, with the hydrophobic segment completely inserted in the bilayer core and the hydrophilic segment mostly protruding into the water phase (Figure S5).

Bilayers were hydrated with TIP3P water and 150 mM sodium chloride (CHARMM36). Box sizes were chosen to allow for ample space for the protruding PEO groups and are summarized in *Supporting Information* Table 1 including other simulation

parameters. Bilayers were then slowly equilibrated using the CHARMM-GUI procedure with restraints. In some cases, waters placed between bilayer leaflets during hydration were manually removed to obtain stable equilibration. Before production runs, the lateral area of the membrane was equilibrated to obtain a converged surface area of the membrane patch (Table S1). In all simulations, the CHARMM36 force field was used.

**Simulation Parameters.** Simulations were run using GROMACS (2020) with a timestep of 2 fs, Verlet cutoff-scheme, electrostatics and LJ interactions cutoff at 1.2 nm, and PME long-range electrostatics.<sup>54</sup> Simulations were run NPT ensemble using a Nose–Hoover thermostat and semi-isotropic Parrinello–Rahman pressure coupling for a (laterally) tensionless membrane at 1 bar water pressure. Temperature coupling was done with the Nose–Hoover algorithm with 1 ps coupling time constant. Simulation temperatures, trajectory length, and the number of replicates are summarized in Table S1. Atom positions were saved every 20 ps. Example bilayer structure, topology, force field, and simulation parameters can be found in the *Supporting Information* as a ZIP file.

**Analysis of Simulations.** Density profiles were obtained using gmx density (GROMACS) with the bilayer centered in the simulation box from the last 100 ns of the simulation trajectory. Polymer end-to-end distances was calculated using gmx polystat (GROMACS) from the last 100 ns of the simulation trajectory. The membrane elastic modulus  $K_A$  was estimated from the thermal bilayer area fluctuations<sup>55</sup>

$$K_A = k_B T \frac{a_0}{\langle (a - a_0)^2 \rangle} \quad (1)$$

where  $a_0$  is the average lateral bilayer area and  $\langle (a - a_0)^2 \rangle$  are the mean squared area fluctuations measured from the size of the simulation box over the full trajectory after equilibration (Table S1). Bilayer defect densities were measured using PackMem (<https://packmem.ipmc.cnrs.fr/>) with PEO-*b*-PBD added as PDB (hydrophobic) and PEO (hydrophilic) molecules.<sup>37</sup> The membrane defect sizes were calculated by the PackMem script for “deep” defects below the headgroup interface. The cumulative defect size from each frame was averaged over the trajectory. From a 200 to 400 ns long trajectory after at least 60 ns equilibration (Table S1) for each membrane composition, the resulting distribution was obtained, and the average defect size was calculated. To check if the defect distribution was equilibrated, the trajectory was binned into three equally sized segments, and defect densities were calculated for each segment. Within 10% similar results for each segment indicated an equilibrated defect density.

Statistical uncertainties in the mean values of packing defects, elastic modulus, and membrane thickness were estimated using the blocking analysis implemented in pyblock (<http://github.com/jsspencer/pyblock>) with block sizes chosen to remove the effect of correlation from the data set.<sup>56,57</sup> The used block sizes resulted in 10–50 datapoints for both elastic modulus and defect density calculations. Further analysis was performed using MDAnalysis 0.20.1,<sup>58,59</sup> NumPy 1.18.1 using Python 3.7.<sup>60</sup> Trajectories were visualized using VMD (1.9.3).

**Adsorption and Insertion times.** A single peptide was positioned about 3.5 nm above the membrane normal in an initially alpha helical configuration (initial coordinates generated using open-source pymol v. 2.4.0 <https://github.com/schrodinger/pymol-open-source>) fully immersed in the water phase. Typically, within the first 50–100 ns, peptides lost most of their alpha helical structure, generating a different starting conformation for each simulation run, diffused through the water phase, and finally adsorbed to the membrane–water interface. Membrane adsorption was quantified as a measured center of mass distance below 2 nm from the bilayer core and defined as the measurement of  $t_{ads}$ . Complete insertion was detected by crossing of the membrane midplane by the peptide center of mass.

**PCA Calculation.** Principal component analysis (PCA) conformational landscape was calculated using PyEMMA 2.5.7 from backbone torsion angles.<sup>61</sup> For comparison of the conformational space, the same PCA basis obtained for DOPC was also used for 10 mol % PEO-

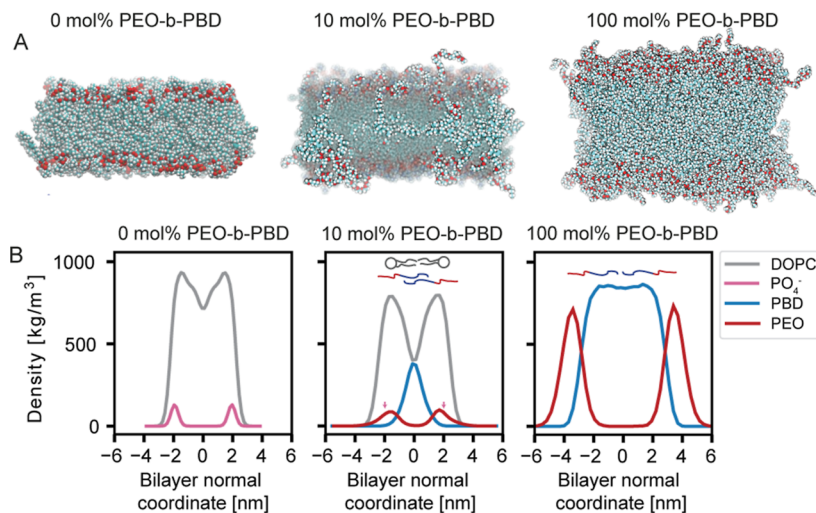


**Figure 1.** Amphiphile location in a hybrid lipid/polymer membrane varies as a function of lipid/polymer ratio. (A) Snapshots from an all-atom simulation of DOPC bilayers containing increasing amounts of PEO-*b*-PBD ( $\text{PEO}_{14}$ -*b*-PBD<sub>22</sub> MW = 1.8 kDa). (B) Spatial density profile of amphiphiles, displayed normal to the bilayer surface and with contributions of DOPC, PEO, and PBD shown separately for increasing fraction of PEO-*b*-PBD in the membrane. Distribution of DOPC phosphate headgroup is shown in the left most density plot, and small arrows in the middle panel show the average phosphate location. Structure and elastic properties of DOPC membranes blended with low-MW PEO-*b*-PBD.

*b*-PDB hybrids. Representative samples were then drawn from *k*-mean clusters corresponding to the states shown in Figure 2E,F.

## EXPERIMENTS

**Materials.** DOPC and 1,2-dioleoyl-*sn*-glycero-3-phosphoethanolamine-*N*-(7-nitro-2,1,3-benzoxadiazol-4-yl) (ammonium salt) (18:1 NBD PE) were obtained from Avanti Polar Lipids. Poly(ethylene oxide)-*b*-poly(butadiene) diblock copolymers PEO14-*b*-PBD22 (1.8 kDa) and PEO24-*b*-PBD36 (3.5 kDa) were obtained from Polymer Source. Sodium dithionite, chloroform, bovine serum albumin (BSA), and phosphate-buffered saline (PBS) were purchased from Sigma-Aldrich.

**Hybrid Vesicle Preparation and Size Measurements.** Hybrid DOPC and PEO-*b*-PBD large unilamellar vesicles (LUVs) composed were prepared as described previously with 0.2 mol % 18:1 PE-NBD. Briefly, lipids and polymers were dissolved in chloroform or methylene chloride, respectively.<sup>17,62</sup> Dissolved lipids and polymers were mixed in a 20 mL glass vial at indicated mol %. Chloroform was evaporated using a stream of nitrogen to form a thin film on the wall of a glass vial and then incubated under vacuum (~0.8 bar) at 25 °C for >4 h. Films were gently rehydrated in 1 mL of PBS, pH 7.4 to achieve a concentration of 5 mM total membrane amphiphile. Vials were capped tightly and incubated at 60 °C overnight. Vesicles were vortexed and extruded with 7 passes through an Avanti minieextruder with a 100 nm polycarbonate filter (Avanti Polar Lipids).

Resulting vesicle size distribution was measured by dynamic light scattering. In these experiments, extruded vesicles were diluted to 0.01 mM total amphiphile in PBS. Dynamic light scattering measurements were collected with the Zetasizer Ultra Blue system (Malvern Instruments Ltd., Malvern, UK) using a He–Ne (633 nm) laser. The resulting size distribution confirmed the vesicle diameters to be centered around 100 nm (Figure S6A). Micelles were only present in the positive micelle control (addition of 1% Triton X-100 before data collection, Figure S6B).

**Dithionite NBD Quenching Membrane Permeability Assay.** 1 M Sodium dithionite was prepared fresh immediately prior to experiments in 1X PBS, pH 7.4. Small unilamellar vesicles were diluted to 2.5 mM in PBS, and NBD fluorescence was measured at excitation 463 nm, emission 536 nm using a kinetic scan on a Cary eclipse fluorescence spectrometer (Agilent) which induces only minimal photobleaching (Figure S7). Sodium dithionite was added to a final concentration of 75 mM after 1 min of kinetic scan. The scan was continued for 20 min further to measure the rate of NBD

quenching in the membrane inner leaflet. Normalized NBD fluorescence was calculated by dividing the fluorescence intensity by the fluorescence intensity immediately after outer leaflet quenching. NBD quenching rate was calculated as %/min.

**Electroformation of GUVs.** Giant unilamellar vesicles (GUVs) were formed through electroformation using the Nanonion Vesicle Prep Pro (Nanonion Technologies). Amphiphiles were mixed at various mol % concentrations in chloroform to form a 20 mM total amphiphile stock; 10 μL of stock was dried onto the conductive side of a Nanion ITO slide and placed in a vacuum oven for >30 min. Slides were hydrated with 200 μL of 280 mOsm sucrose, and GUVs were formed using the standard preparation protocol.

**Micropipette Aspiration of Hybrid Membranes.** Borosilicate pipettes were pulled on a Flaming/Brown micropipette puller (model p-1000, Sutter Instruments) and cut to ~5 μm in diameter on a microforge (model MF-900, Narishige). Pipettes were filled with PBS solution with 1 wt % BSA and attached to a custom aspiration station mounted on a Nikon Ti2 inverted microscope. This setup was equipped with a manometer, a Validyne pressure transducer (model DP 15-32, Validyne Engineering Corp), a digital pressure readout, and micromanipulators (model WR-6, Narishige). A syringe was connected to the manometer, which was used to apply suction pressure to electroformed GUVs in ~1 cm H<sub>2</sub>O increments. GUVs were prestretched for ~30 s and then aspirated in steps with ~5 s allowed for equilibration before subsequent aspiration steps. Images were analyzed in ImageJ to determine the vesicle diameter, pipette diameter and membrane extension, which were then used to calculate the  $K_{app}$  of each population of vesicles through the Laplace law. An example measurement is shown in Figure S8.

## RESULTS AND DISCUSSION

**All-Atom MD Model Development.** Polyethylene oxide-*b*-polybutadiene diblock copolymers ( $\text{PEO}_{14}$ -*b*-PBD<sub>22</sub>, 1.8 kDa), hereafter referred to as PEO-*b*-PBD, were parametrized for all-atom MDs simulations. The polymers were assembled into bilayers and equilibrated to a fluid bilayer phase (see Methods). After a total simulation time of 1.2 μs, the area per polymer chain was found to be close to 0.87 nm<sup>2</sup>. This area agrees well to a scaling relation between the area per chain and the molecular weight of the hydrophobic block ( $MW_h$ )<sup>1-α</sup>,<sup>27</sup> which predicts a polymer chain area of about 0.8 nm<sup>2</sup> for the estimate  $α = 0.6$  obtained by fitting of experimental and

**Table 1.** Summary of Area Expansion Moduli (Elastic Moduli) from Experimental Data and Simulations<sup>a</sup>

| molar ratio of DOPC:polymer     | $K_{app}$ [mN/m] (exp) | $K_a$ [mN/m] (sim) | $d_{pp}$ [nm] (sim) | $d_{EE}$ [nm] (sim) | $d_{EE-PEO}$ [nm] (sim) |
|---------------------------------|------------------------|--------------------|---------------------|---------------------|-------------------------|
| DOPC/PEO- <i>b</i> -PBD 1.8k MW |                        |                    |                     |                     |                         |
| 100:0                           | 196 ± 17               | 256 ± 17           | 3.9 ± 0.01          | n.d.                | n.d.                    |
| 90:10                           | 113 ± 4                | 122 ± 20           | 4.2 ± 0.02          | 3.4 ± 0.02          | 1.9 ± 0.01              |
| 80:20*                          | 71 ± 11                | 102 ± 40           | 4.5 ± 0.02          | 3.7 ± 0.01          | 2.0 ± 0.01              |
| 0:100                           | 103 ± 5                | n.d.               | n.d.                | 4.0 ± 0.01          | 2.1 ± 0.01              |
| DOPC/PEO- <i>b</i> -PBD 3.5k MW |                        |                    |                     |                     |                         |
| 90:10                           | n.d.                   | 164 ± 5            | 4.7 ± 0.02          | 5.0 ± 0.01          | 2.7 ± 0.01              |
| 80:20                           | 170 ± 7                | n.d.               | n.d.                | n.d.                | n.d.                    |

<sup>a</sup>Simulation data for DOPC phosphate-to-phosphate distance,  $d_{pp}$ , PEO-*b*-PBD end-to-end distance,  $d_{EE}$  and PEO end-to-end distance  $d_{EE-PEO}$ . Experimental data for 100:0 and 75:25 DOPC/PEO-*b*-PBD 1.8k adapted from ref 17. Experiments were conducted at 296 K. Experiments reported the “apparent” elastic modulus  $K_{app}$ , which is lower than the real bilayer elastic modulus  $K_a$ . \*The experimental value for 75:25 is compared to 80:20 simulation. ± indicate std. err. determined from blocking analysis for the simulations (see Methods) or experimental repeats (aspiration of single GUVs) with  $n > 15$ . N.d. abbreviates “not determined.”

simulation data for another PBD parametrization.<sup>18</sup> After this initial validation of our model, we assembled DOPC phospholipid bilayers containing 10 and 20 mol % PEO-*b*-PBD (**Figure 1A**) and set out to investigate the impact of polymer content on the bilayer structure.

We examined the phase state of the simulated hybrid membranes. Visual inspection of the 200–500 ns long trajectories revealed that PEO-*b*-PBD polymers form nanoscopic clusters in coexistence with individual PEO-*b*-PBD monomers embedded in a DOPC bilayer (**Movie M1**). We analyzed the cluster size over time (**Figure S1A**) and found that the cluster size is dynamic, with frequent changes between small and large clusters, indicative of a single fluid phase instead of a phase-separated system. This observation agrees with our previous experiments using fluorescently tagged lipids which showed that the particular compositions of DOPC/PEO-*b*-PBD investigated here form a single phase.<sup>17</sup> Similar results were found for PEO-*b*-PBD polymer hybrids with a different lipid.<sup>12</sup> Accordingly, we expect our computational model to reflect a single-phase membrane with transient cluster formation.

Surprisingly, we observed that the diblock copolymer chains changed their preferred location in a bilayer membrane as a function of the polymer content. Specifically, at a low polymer content of 10 mol % PEO-*b*-PBD, the polymers appear to insert deeply and associate closely with the membrane core, where the DOPC density is the lowest (**Figure 1B**). Examining the locations of the hydrophobic PBD and hydrophilic PEO blocks separately, we find that at 10 mol % PEO-*b*-PBD inclusion, the PBD chains are confined within the hydrophobic core of the bilayer (blue curve, **Figure 1B**) in a tightly packed, partially interdigitated configuration (see polymer end-to-end distance,  $d_{EE}$ , **Table 1** and corresponding density distributions in **Figure 1B**). Because the studied PEO-*b*-PBD polymers are rather short, the deep and compact PBD insertion inevitably collocates the covalently linked PEO chains at a location that just extends to the membrane–water interface. As a result, the membrane thickness of the hybrid membrane with low polymer content matches the approximately 4 nm membrane thickness of the pure phospholipid membrane (see phosphate-to-phosphate DOPC thickness,  $d_{pp}$ , in **Table 1**). At higher concentrations of the polymer, the polymer chains take on a more oriented conformation that spans the membrane. For example, at 100 mol % PEO-*b*-PBD, the hydrophobic PBD chains take on a broader spatial distribution relative to 10 mol % PEO-*b*-PBD and the membrane hydrophobic thickness

increases from about 4 to 6 nm, in line with the expected polymer conformation in bilayer membranes (**Figure 1B**).<sup>27,29</sup> Very recently, experiments using a combination of small-angle X-ray scattering and cryo-electron tomography found a hydrophobic thickness of 6.6 nm for 100 mol % PEO-*b*-PBD vesicles.<sup>30</sup>

The observed PEO configuration is very different from when PEO is anchored to lipid surfaces, where PEO adopts mushroom or brush configurations in the water phase above the membrane surface.<sup>31</sup> To understand these differences better, it is instructive to compare the PEO subunit end-to-end distance to that of a free PEO chain of equal molecular weight in solution. The obtained values  $d_{EE-PEO}$  (**Table 1**) remain below or at the end-to-end distance of 2.1 nm measured in solution,<sup>32</sup> meaning that the studied low-MW PEO chains in hybrid membranes are in a more compact configuration than in solution and are not significantly stretched in pure polymer membranes. The absence of stretching is distinctively different from the mushroom-to-brush transition of the PEO polymer grafted to lipid membranes via anchor lipids, where at high densities, PEO adopts a larger end-to-end distance than in solution.<sup>31</sup> Simulations of a higher-MW polymer analogue, PEO-*b*-PBD (3.5 kDa, PEO24-*b*-PBD46), showed that PEO chains protrude into the water phase with higher probability than the lower-MW polymer, giving a more typical “PEGylated” or mushroom, polymer configuration of the membrane surface (**Table 1** and **Figure S1B**). This is consistent with the  $d_{EE-PEO}$  value (**Table 1**) being closer to the value in solution of 2.8 nm.<sup>32</sup> Our observation of a varying PEO location in membranes adds to the idea that even if PEO is usually considered hydrophilic, it can have amphiphilic character.<sup>33</sup> In line with our results, previous groups have also observed PEO localization at the lipid–water interface both experimentally and in silico.<sup>34–36</sup>

We used micropipette aspiration of hybrid GUVs to experimentally validate the confined polymer conformations in membranes that occur when a low-MW polymer (PEO-*b*-PBD 1.8 kDa) is included at low concentrations (10–20 mol %). Because the PEO portions of polymer chains are pulled into the membrane in this condition, we expect surface tension and a correlated area expansion modulus to be reduced relative to either pure phospholipid or pure polymer membranes.<sup>28,29</sup> We measured the elastic modulus from simulation box fluctuations and found that it indeed follows this expectation, with an almost 2-fold decrease in  $K_a$  from 196 ± 17 mN/m for pure DOPC to 113 ± 4 mN/m for 10 mol % PEO-*b*-PBD. The

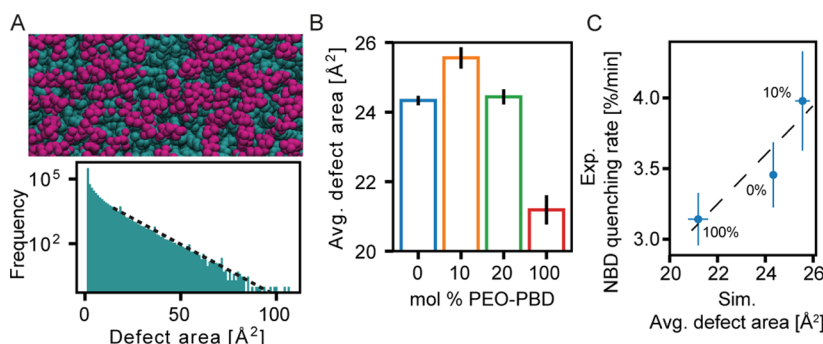


**Figure 2.** Polymer inclusion in lipid membranes generates transient packing defects. (A) Top view of the membrane where cyan regions represent hydrophobic residues that are accessible from the water phase and magenta residues represent lipid headgroups. Defect density follows an exponential distribution (dashed line). (B) Average defect areas obtained from the defect distribution are shown as bar graphs for varying membrane compositions. (C) Membrane permeability measured by NBD quenching by dithionite correlated with the simulation defect area. Fraction of PEO-*b*-PBD is indicated as a percentage next to datapoints. All error bars indicate standard error. ( $n = 3$  experimental repeats, simulation errors estimated from blocking analysis).

area expansion moduli (elastic modulus) computed from equilibrium box fluctuations agrees with micropipette aspiration experiments on single-phase, giant unilamellar, hybrid vesicles (Table 1), further corroborating our simulation model. Similarly, our measurements of the elastic modulus for membranes containing the higher-MW polymer (PEO-*b*-PBD 3.5k Table 1), which appears stiffer and support our simulation-derived results that the higher-MW polymers take on a more linear, membrane-spanning conformation.

In summary, our computational model of hybrid DOPC/PEO-*b*-PBD membranes compares well to experimentally determined metrics of phase state and elastic moduli. Our simulations reveal that the membranes form a uniform phase, and that low-MW PEO-*b*-PBD takes on an unexpected, membrane-immersed conformation when it is incorporated at low polymer content levels in phospholipid membranes. This conformation reduces the surface tension and area expansion modulus of the resulting membranes that are validated by experimental measurements. Increasing the PEO-*b*-PBD MW or total polymer content leads to a more expected mushroom or “PEGylated” conformation. Taken together, our simulations support the existence of a diverse structural space for mixtures of polymer and phospholipid amphiphiles, one that varies based on the MW of the diblock copolymer used as well as the concentration at which it appears in a lipid membrane.

**Polymer Inclusion and Reduced Membrane Cohesion Leads to Transient Packing Defects.** We wondered what changes in structural dynamics might accompany changes in polymer concentration in hybrid bilayer membranes. We hypothesized that low amounts of PEO-*b*-PBD may introduce transient membrane packing defects, a parameter that describes thermally activated water insertion sites (or defects) in the bilayer. As studied previously for pure phospholipid systems,<sup>37–39</sup> density fluctuations in the lipid headgroup region led to transient exposure of the hydrophobic core to the surrounding aqueous solvent. We quantified packing defects using PackMem which identifies defects based on solvent accessibility of the hydrophobic core.<sup>37</sup> In our simulations, we observed that packing defects of varying sizes appear on the surface of hybrid bilayer membranes (Figure 2A). Packing defects appeared most frequently for DOPC membranes containing 10 mol % PEO-*b*-PBD and least often for pure PEO-*b*-PBD membranes (Figure 2B). Some defects became

relatively large ( $\gg 1 \text{ nm}^2$ ) even on the relatively short simulation timescale of hundreds of nanoseconds. On much longer length scales and timescales of minutes, like those reflecting experiments, we expect that even larger defects would occasionally appear, spanning both leaflets to form water-filled pores. Such transient pores should lead to an increase in membrane permeability for hydrophilic solutes. To confirm the presence of such large defects, we conducted experiments measuring LUV permeability to dithionite, which is a +2 charged hydrophilic molecule. Dithionite forms irreversible complexes with the lipid conjugated dye NBD and quenches NBD fluorescence. After a rapid quenching of NBD located in the outer vesicle surface, the following slow decreases in NBD fluorescence is indicative of dithionite crossing the membrane to quench NBD located on the inner membrane leaflet.<sup>40</sup> Consistent with the simulation data, our measurements of dithionite-NBD quenching indicate that membrane permeability is increased at 10 mol % PEO-*b*-PBD and is the lowest in pure PEO-*b*-PBD (Figure S2). Within error, the correlation between the experimental NBD quenching rates and the simulation defect density is good (Figure 2C). Our NBD quenching results are also consistent with increased proton permeability in hybrid membranes at intermediate polymer concentrations.<sup>14,41</sup> However, we do note some limitations of our comparison between experiment and simulation; the measured membrane permeability does not probe defect density directly. Additionally, we note the slow relaxation of the 100 mol % polymer membrane simulation, which might not be fully equilibrated. Nevertheless, these results add to the idea that polymer incorporation leads to a nonmonotonic enhancement of packing defects in 10 mol % PEO-*b*-PBD hybrid membranes.

**Low Amounts of Diblock Copolymer Inclusion in Hybrid Membranes Enhances Peptide Insertion Rates.** In pure lipid membranes, packing defects have previously been shown to enhance peptide adsorption and insertion.<sup>37,42–44</sup> We hypothesized that in a similar way, packing defects would enhance peptide/membrane insertion rates in hybrid membranes. We studied polyleucine “host” peptides of the sequence ac-LLLLXLLLL-nme (L8X) that favorably interact with the hydrophobic lipid bilayer core. Previous computational studies of lipid membrane/peptide interactions have systematically varied X to every other amino acid and calculated the free energy of adsorbed and inserted states,<sup>45</sup> making L8X a

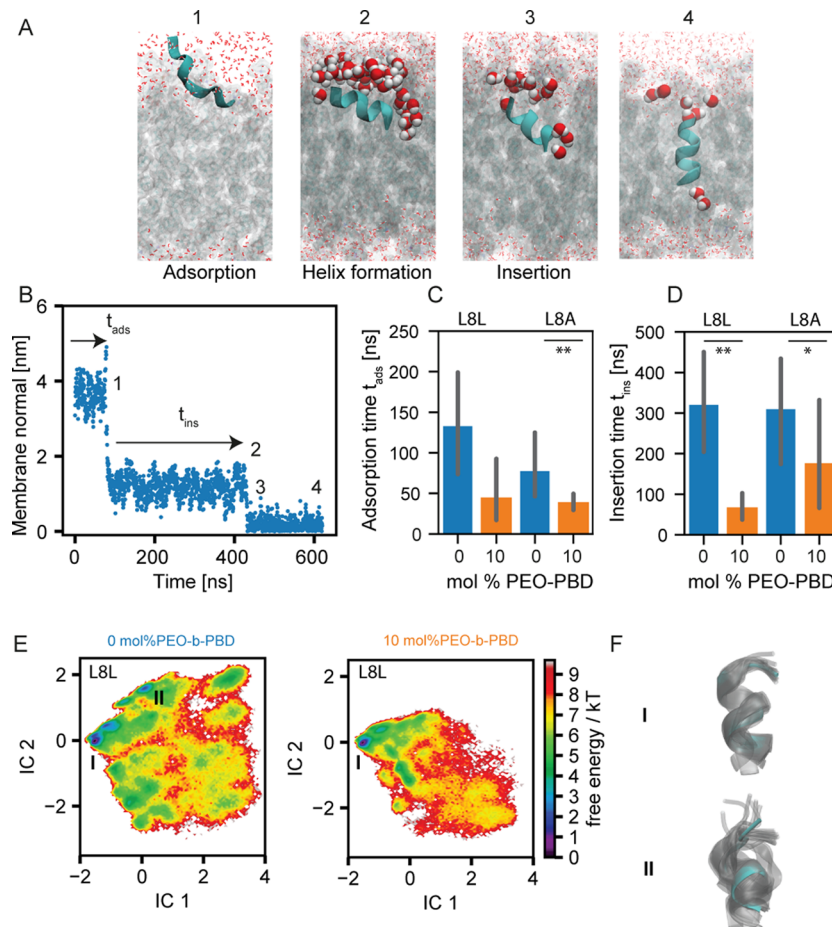


**Figure 3.** (A) Representative simulation snapshots for the timepoints 1–4. Peptide L8L is shown in cyan, DOPC lipids in diffuse gray, and waters as small white and red spheres, with waters within 5 Å of L8L as large spheres. (B) Sample trajectory for the peptide sequence LLLLLLLL (L8L) shows distance from the DOPC membrane midplane. Timepoints 1–4 correspond to panel A above. (C,D) Average adsorption time  $t_{ads}$  and insertion time  $t_{ins}$  for L8L and L8A in pure DOPC (blue) and 10 mol % PEO-*b*-PBD (orange) membranes. Bar plots show mean and standard deviation, significance calculated from Students *t*-test, \*\**p* < 0.01, \**p* < 0.05, *n* = 9 trajectories. (E) Pseudo-free energy landscape for the first two principal components. (F) Corresponding snapshots that were sampled from states I, II are shown on the right with cyan structures and gray overlays of additional samples.

suitable starting point for our investigations. Here and in the previous study, the simulation kinetics were sped-up by using an elevated temperature of 80 °C. We obtained 600 ns of simulation data per peptide with nine replicates. This protocol was previously shown to produce a similar insertion energy landscape as lower temperature simulations and experiments.<sup>46,47</sup> Additionally, we checked the polymer distribution at 80 °C and found the same deeply inserted configuration for 10 mol % PEO-*b*-PBD (Figure S2B), validating our elevated temperature simulation protocol.

Next, we studied the interaction of these peptides with the hybrid membranes. Initially, we placed a single peptide of sequence ac-LLLLLLLLL-nme (L8L) above the membrane. Over time, the peptide diffused in the water phase and eventually adsorbed at the membrane interface (indicated by 1 in Figure 3A). At the membrane–water interface, the peptide developed an alpha helical structure and then inserted into the bilayer in a trans-membrane configuration (2 Figure 3A). We measured the time,  $t_{ads}$ , of initial adsorption of the unstructured peptide from the water phase and insertion time after adsorption,  $t_{ins}$ , from the distance of the peptide center of mass to the membrane midplane (Figure 3B). Both adsorption and insertion times were reduced in membranes containing 10

mol % PEO-*b*-PBD relative to 100% DOPC (Figure 3C,D) by a factor between 1.5 and 4. The effect was most significant for the insertion time, which is expected because the adsorption time probes both the peptide-membrane interactions and diffusion in the water phase, making it a less sensitive measure. We note that on the simulation timescale, peptide insertion into 100 mol % PEO-*b*-PBD membranes was never observed, demonstrating the nonmonotonic effects polymer addition have on peptide insertion kinetics. Next, we studied the peptide sequence L8A (ac-LLLLALLLL-nme). The free-energy difference between the membrane interface and the inserted state was determined to be -3.4 kcal/mol, which is close to that of L8L with a free energy difference of -4.1 kcal/mol ± 1 kcal/mol.<sup>45</sup> Though free energy differences between the membrane interface and inserted state were similar for both peptides, L8A exhibited smaller adsorption times to the DOPC membrane interface compared to L8L. Interestingly we also found increased insertion rates of L8A with the addition of polymer to the membranes but with a smaller magnitude compared to L8L (Figure 3C,D). L8L displayed an almost 4-fold increase in the insertion rate relative to L8A when hybrid membranes contained 10 mol % polymer. Hence, we hypothesized that L8L and L8A make an interesting

comparison as the central alanine might modify the peptide insertion dynamics.

To understand the differences in insertion kinetics of L8L and L8A into membranes with increased polymer content, we first considered the role of membrane defects in peptide insertion. We considered a simplified model where peptide insertion requires the appearance of a suitable defect size. In this model the insertion rate is approximated as  $k_{\text{insert}} = \frac{1}{t_{\text{ins}}} \sim P_{\text{def}}(A > A_0) = \exp(-A_0\lambda)$ , where  $P_{\text{def}}$  is the probability to find a defect larger than  $A_0$ . Within this model,  $A_0$  should be close to the peptide footprint on the membrane. We assume the same defect distribution for both peptides which is characterized by the defect constant  $1/\lambda$  calculated in the absence of the peptide (Figure 2B). We find for L8L,  $A_{0,\text{L8L}} \approx 4.8$  nm, and for L8A,  $A_{0,\text{L8A}} \approx 1.8$  nm. These values should be compared to the real footprint of both peptides which is  $A_{\text{real}} \approx 1.7$  nm calculated from the alpha helical geometry. The good agreement between  $A_{0,\text{L8A}}$  and  $A_{\text{real}}$  and the larger value of  $A_{0,\text{L8L}}$  suggests that the enhancement of L8A kinetics in the presence of the polymer is mainly due to packing defects, while additional effects must be at play for L8L insertion that further speeds its insertion rate.

**Conformal Selection of Peptides at Membrane–Water Interface.** To understand what additional factors might contribute to L8L insertion kinetics into hybrid membranes with 10 mol % polymer, we studied the peptide conformational space. Here, PCA was used to quantify the peptide backbone torsion angles from the simulated trajectories. Both for pure DOPC and 10 mol % PEO-*b*-PBD, we observed a pronounced preference for the same alpha helical conformation (indicated with a I in Figure 2E). However, we also observed a second, less favorable conformation that was only observed in pure DOPC membranes, corresponding to a partially unfolded state (II Figure 2E). As only the fully helical conformation I was observed to insert into the bilayer core, state II corresponds to a “misfolded” state that could not insert into the membrane. Thus, the addition of the polymer into the DOPC membrane appears to suppress state II and subsequently contributes to faster L8L membrane insertion.

Further analysis then showed that conformation II only exists at the membrane–water interface. We wondered if membrane interface state II is simply not sampled because of the faster insertion of the peptide in hybrid membranes. However, we observed that transitions between I and II in DOPC membranes occur on a timescale at least an order of magnitude faster than peptide insertion, giving ample time for sampling state II if it is present in the hybrid membrane. While we did not further study the exact molecular mechanism by which state II is suppressed in this study, we note that state II had the highest separation from the membrane midplane of all observed states. It appears as if the less cohesive, polymer blended, membrane–water interface allows deeper integration of this peptide even before final transmembrane insertion, and in this way, low amounts of polymer inclusion stabilize the folded state of a peptide. PCA analysis of L8A showed an overall more similar conformational landscape between DOPC and 10 mol % PEO-*b*-PBD membranes, corroborating that membrane defects play the predominant role in enhancing L8A membrane insertion rates (Figure S3). Taken together, our results show that inclusion of small fractions of low molecular PEO-*b*-PBD into DOPC membranes enhances

peptide insertion kinetics by at least two different mechanisms: induction of packing defects that allows passage of a peptide to the membrane core and conformational selection of peptides that favors folding at the membrane–water interface.

Our study was limited to a small peptide sequence and individual, lone peptides. Certainly, sequence-specific effects might be expected, and additional effects might come into play at higher peptide concentrations. For example, the insertion of multipass transmembrane protein helices has been shown to be cooperative.<sup>3</sup> The extent to which such cooperative insertion events might be further enhanced at defect sites poses an interesting question for future studies. It also remains to be seen if enhancement of peptide adsorption rates at defect sites is relevant for the membrane association of peripheral membrane proteins.

## CONCLUSIONS

In this work, we have studied DOPC and PEO-*b*-PBD hybrid membranes using all-atom MD simulations, focusing on a 1.8 kDa MW PEO-*b*-PBD and membranes with small (10 mol %) polymer content. Our computational hybrid membrane model was validated against available and new experimental data. In this way, we provide evidence for deep insertion of low-MW PEO-*b*-PBD (1.8 kDa) into the lipid bilayer which locates PEO at the membrane–water interface. This configuration decreases membrane cohesion, which reduces its elastic modulus and leads to a rise in packing defects. The effects of low-MW PEO-*b*-PBD might be considered similar to the effects of detergent on lipid bilayers. However, in strong contrast to typically used detergents, pure 1.8k PEO-*b*-PBD polymer prefers lamellar phases and thus forms a stable hybrid lipid/polymer membrane at any concentration. This eliminates the need to wash away the detergent or possible interference of free detergent with, for example, cell-free expression activity. Focusing on a membrane composition with low polymer content, we then studied the interactions of two different peptides with the resulting membrane. The studied peptides show very similar alpha helical structures in pure lipid and hybrid membranes, exemplifying the biocompatibility of lipid/polymer hybrid membranes. Additionally, we have shown evidence for quenching of high-energy “misfolded” conformational states for one peptide (L8L) when polymer is included in the membrane. Together with packing defects, membrane-induced changes in the peptide conformational space contribute to increased peptide insertion rates in hybrid membranes containing low-MW PEO-*b*-PBD. Our results suggest that the inclusion of small fractions of polymer might lead to large changes in peptide adsorption and insertion kinetics via a generic mechanism of induction of water defect sites in the bilayer. As a result, this study expands the understanding of the role polymers may play in hybrid membrane systems and should inform the exploration and design of an expanded repertoire of biocompatible polymers for incorporation into lipid membranes.

## ASSOCIATED CONTENT

### SI Supporting Information

The Supporting Information is available free of charge at <https://pubs.acs.org/doi/10.1021/acs.biomac.2c00936>.

Overview over the performed simulations; size of the largest PEO-*b*-PBD clusters determined by DBSCAN; example kinetic traces for NBD dithionite quenching

membrane permeability LUV assay; pseudo free energy for L8A peptide obtained by PCA analysis for DOPC and 10 mol% PEO-*b*-PDB membranes; parametrization of a PBD monomer; initial configuration of 20 mol % PEO-*b*-PDB; extruded vesicle size distribution as measured by DLS; NBD photobleaching control in the absence of sodium dithionite; and sample aspiration curve showing the strain-tension relationship; and CGneFF result for the 1,2 PB trimer ([PDF](#))  
Example bilayer structure, topology, force field, and simulation parameter for use with GROMACS 2020 and example simulation ([ZIP](#))

PEO-*b*-PBD polymers forming nanoscopic clusters in coexistence with individual PEO-*b*-PBD monomers embedded in a DOPC bilayer ([MOV](#))

## AUTHOR INFORMATION

### Corresponding Author

Neha P. Kamat — Department of Biomedical Engineering, Northwestern University, Evanston, Illinois 60208, United States; Center for Synthetic Biology, Northwestern University, Evanston, Illinois 60657, United States;  [orcid.org/0000-0001-9362-6106](#); Email: [nkamat@northwestern.edu](mailto:nkamat@northwestern.edu)

### Authors

Jan Steinkühler — Department of Biomedical Engineering, Northwestern University, Evanston, Illinois 60208, United States

Miranda L. Jacobs — Department of Biomedical Engineering, Northwestern University, Evanston, Illinois 60208, United States

Margrethe A. Boyd — Department of Biomedical Engineering, Northwestern University, Evanston, Illinois 60208, United States

Citlayi G. Villaseñor — Department of Biomedical Engineering, Northwestern University, Evanston, Illinois 60208, United States

Sharon M. Loverde — Department of Chemistry, College of Staten Island, The City University of New York, Staten Island, New York 10314, United States; Present

Address: Ph.D. Program in Biochemistry, Ph.D. Program in Chemistry, and Ph.D. Program in Physics, The Graduate Center of the City University of New York, New York, New York 10016, United States

Complete contact information is available at:

<https://pubs.acs.org/10.1021/acs.biomac.2c00936>

### Author Contributions

The manuscript was written by J.S., S.M.L., and N.P.K. Simulations were designed and performed by J.S. and S.M.L. Experiments were designed and performed by J.S., M.L.J., M.A.B., and N.P.K. All authors analyzed the results.

### Notes

The authors declare the following competing financial interest(s): N.P.K and J.S. are inventors on a U.S. provisional patent submitted by Northwestern University that covers organizing cell-free expressed membrane proteins in synthetic membranes.

## ACKNOWLEDGMENTS

J.S. would like to acknowledge Markus Mietten and João R. Robalo for their advice on MD simulations. This research was

supported in part by the National Science Foundation under grant no. 2145050 (N.P.K.), 1844336 (N.P.K., J.S.), the Air Force Office of Scientific Research (FA9550-19-1-0039, N.P.K., C.G.V.), and the Molecular Biophysics Training Program funded by the National Institute of General Medical Sciences (NIGMS) of the National Institutes of Health (5T32 GM008382) (C.G.V.), NSF grant DMR-1750694 (S.M.L.), and through the computational resources and staff contributions provided for the Quest high performance computing facility at Northwestern University which is jointly supported by the Office of the Provost, the Office for Research, and Northwestern University Information Technology.

## REFERENCES

- (1) Chwastek, G.; Surma, M. A.; Rizk, S.; Grosser, D.; Lavrynenko, O.; Rucińska, M.; Jambor, H.; Sáenz, J. Principles of Membrane Adaptation Revealed through Environmentally Induced Bacterial Lipidome Remodeling. *Cell Rep.* **2020**, *32*, 108165.
- (2) Harris, N. J.; Reading, E.; Ataka, K.; Grzegorzewski, L.; Charalambous, K.; Liu, X.; Schlesinger, R.; Heberle, J.; Booth, P. J. Structure Formation during Translocation-Unassisted Co-Translational Membrane Protein Folding. *Sci. Rep.* **2017**, *7*, 1–15.
- (3) Choi, H. K.; Min, D.; Kang, H.; Shon, M. J.; Rah, S. H.; Kim, H. C.; Jeong, H.; Choi, H. J.; Bowie, J. U.; Yoon, T. Y. Watching Helical Membrane Proteins Fold Reveals a Common N-to-C-Terminal Folding Pathway. *Science* **2019**, *366*, 1150–1156.
- (4) Sanguinini, M.; Baumann, K. N.; Preet, S.; Chia, S.; Habchi, J.; Knowles, T. P. J.; Vendruscolo, M. Complexity in Lipid Membrane Composition Induces Resilience to  $\text{A}\beta 42$  Aggregation. *ACS Chem. Neurosci.* **2020**, *11*, 1347–1352.
- (5) Booth, P. J.; Riley, M. L.; Flitsch, S. L.; Templar, R. H.; Farooq, A.; Curran, A. R.; Chadborn, N.; Wright, P. Evidence That Bilayer Bending Rigidity Affects Membrane Protein Folding. *Biochemistry* **1997**, *36*, 197–203.
- (6) Marsh, D.; Shanmugavadi, B.; Kleinschmidt, J. H. Membrane Elastic Fluctuations and the Insertion and Tilt of  $\beta$ -Barrel Proteins. *Biophys. J.* **2006**, *91*, 227–232.
- (7) Corin, K.; Bowie, J. U. How Bilayer Properties Influence Membrane Protein Folding. *Protein Sci.* **2020**, *29*, 2348–2362.
- (8) Beales, P. A.; Khan, S.; Muench, S. P.; Jeuken, L. J. C. Durable Vesicles for Reconstitution of Membrane Proteins in Biotechnology. *Biochem. Soc. Trans.* **2017**, *45*, 15–26.
- (9) Otrin, L.; Witkowska, A.; Marušić, N.; Zhao, Z.; Lira, R. B.; Kyriakis, F. L.; Hamdi, F.; Ivanov, I.; Lipowsky, R.; Kastritis, P. L.; Dimova, R.; Sundmacher, K.; Jahn, R.; Vidaković-Koch, T. En Route to Dynamic Life Processes by SNARE-Mediated Fusion of Polymer and Hybrid Membranes. *Nat. Commun.* **2021**, *12*, 1–12.
- (10) Le Meins, J. F.; Schatz, C.; Lecommandoux, S.; Sandre, O. Hybrid Polymer/Lipid Vesicles: State of the Art and Future Perspectives. *Mater. Today* **2013**, *16*, 397.
- (11) Fauquignon, M.; Ibarboure, E.; Le Meins, J. F. Membrane Reinforcement in Giant Hybrid Polymer Lipid Vesicles Achieved by Controlling the Polymer Architecture. *Soft Matter* **2021**, *17*, 83.
- (12) Seneviratne, R.; Catania, R.; Rappolt, M.; Jeuken, L. J. C.; Beales, P. A. Membrane mixing and dynamics in hybrid POPC/poly(1,2-butadiene-block-ethylene oxide) (PBd-*b*-PEO) lipid/block co-polymer giant vesicles. *Soft Matter* **2022**, *18*, 1294–1301.
- (13) Go, Y. K.; Leal, C. Polymer-Lipid Hybrid Materials. *Chem. Rev.* **2021**, *121*, 13996–14030.
- (14) Seneviratne, R.; Khan, S.; Moscrop, E.; Rappolt, M.; Muench, S. P.; Jeuken, L. J. C.; Beales, P. A. A Reconstitution Method for Integral Membrane Proteins in Hybrid Lipid-Polymer Vesicles for Enhanced Functional Durability. *Methods* **2018**, *147*, 142–149.
- (15) Marušić, N.; Otrin, L.; Zhao, Z.; Lira, R. B.; Kyriakis, F. L.; Hamdi, F.; Kastritis, P. L.; Vidaković-Koch, T.; Ivanov, I.; Sundmacher, K.; Dimova, R. Constructing Artificial Respiratory Chain in Polymer Compartments: Insights into the Interplay between

- Bo3 Oxidase and the Membrane. *Proc. Natl. Acad. Sci. U.S.A.* **2020**, *117*, 15006–15017.
- (16) Rottet, S.; Iqbal, S.; Beales, P. A.; Lin, A.; Lee, J.; Rug, M.; Scott, C.; Callaghan, R. Characterisation of Hybrid Polymersome Vesicles Containing the Efflux Pumps NaAtm1 or P-Glycoprotein. *Polymers* **2020**, *12*, 1049.
- (17) Jacobs, M. L.; Boyd, M. A.; Kamat, N. P. Diblock Copolymers Enhance Folding of a Mechanosensitive Membrane Protein during Cell-Free Expression. *Proc. Natl. Acad. Sci. U. S. A.* **2019**, *116*, 4031–4036.
- (18) Barden, D. R.; Vashisth, H. Parameterization and atomistic simulations of biomimetic membranes. *Faraday Discuss.* **2018**, *209*, 161–178.
- (19) Chakraborty, K.; Shinoda, W.; Loverde, S. M. Molecular Simulation of the Shape Deformation of a Polymersome. *Soft Matter* **2020**, *16*, 3234–3244.
- (20) Chakraborty, K.; Khatua, P.; Shinoda, W.; Loverde, S. M. Domain Formation in Charged Polymer Vesicles. *Macromolecules* **2021**, *54*, 9258–9267.
- (21) Loverde, S. M.; Klein, M. L.; Discher, D. E. Nanoparticle Shape Improves Delivery: Rational Coarse Grain Molecular Dynamics (RCG-MD) of Taxol in Worm-like PEG-PCL Micelles. *Adv. Mater.* **2012**, *24*, 3823–3830.
- (22) MacCallum, J. L.; Bennett, W. F.; Tieleman, D. Distribution of Amino Acids in a Lipid Bilayer from Computer Simulations. *Biophys. J.* **2008**, *94*, 3393–3404.
- (23) Ash, W. L.; Stockner, T.; MacCallum, J. L.; Tieleman, D. P. Computer Modeling of Poly-leucine-Based Coiled Coil Dimers in a Realistic Membrane Environment: Insight into Helix–Helix Interactions in Membrane Proteins. *Biochemistry* **2004**, *43*, 9050–9060.
- (24) Kandasamy, S. K.; Larson, R. G. Molecular Dynamics Simulations of Model Trans-Membrane Peptides in Lipid Bilayers: A Systematic Investigation of Hydrophobic Mismatch. *Biophys. J.* **2006**, *90*, 2326–2343.
- (25) Gumbart, J.; Chipot, C.; Schulten, K. Free-Energy Cost for Translocon-Assisted Insertion of Membrane Proteins. *Proc. Natl. Acad. Sci. U.S.A.* **2011**, *108*, 3596–3601.
- (26) MacCallum, J. L.; Bennett, W. F. D.; Tieleman, D. P. Partitioning of Amino Acid Side Chains into Lipid Bilayers: Results from Computer Simulations and Comparison to Experiment. *J. Gen. Physiol.* **2007**, *129*, 371–377.
- (27) Bermudez, H.; Brannan, A. K.; Hammer, D. A.; Bates, F. S.; Discher, D. E. Molecular Weight Dependence of Polymersome Membrane Structure, Elasticity, and Stability. *Macromolecules* **2002**, *35*, 8203–8208.
- (28) Rawicz, W.; Olbrich, K. C.; McIntosh, T.; Needham, D.; Evans, E. A. Effect of Chain Length and Unsaturation on Elasticity of Lipid Bilayers. *Biophys. J.* **2000**, *79*, 328–339.
- (29) Discher, D. E.; Eisenberg, A. Polymer Vesicles. *Science* **2002**, *297*, 967–973.
- (30) Seneviratne, R.; Coates, G.; Xu, Z.; Cornell, C.; Thompson, R.; Sadeghpour, A.; Maskell, D.; Jeuken, L.; Rappolt, M.; Beales, P. High Resolution Membrane Structures within Hybrid Lipid-Polymer Vesicles Revealed by Combining X-Ray Scattering and Electron Microscopy. *2022*, ChemRxiv:4rfqf. <https://chemrxiv.org/engage/chemrxiv/article-details/6334b044e665bd5395161f64> (accessed Oct 10, 2022).
- (31) Hristova, K.; Needham, D. The Influence of Polymer-Grafted Lipids on the Physical Properties of Lipid Bilayers: A Theoretical Study. *J. Colloid Interface Sci.* **1994**, *168*, 302–314.
- (32) Sherck, N.; Webber, T.; Brown, D. R.; Keller, T.; Barry, M.; DeStefano, A.; Jiao, S.; Segalman, R. A.; Fredrickson, G. H.; Shell, M. S.; Han, S. End-to-End Distance Probability Distributions of Dilute Poly(Ethylene Oxide) in Aqueous Solution. *J. Am. Chem. Soc.* **2020**, *142*, 19631–19641.
- (33) Israelachvili, J. The Different Faces of Poly(Ethylene Glycol). *Proc. Natl. Acad. Sci. U.S.A.* **1997**, *94*, 8378–8379.
- (34) Liu, Y.; Agudo-Canalejo, J.; Grafmüller, A.; Dimova, R.; Lipowsky, R. Patterns of Flexible Nanotubes Formed by Liquid-Ordered and Liquid-Disordered Membranes. *ACS Nano* **2016**, *10*, 463–474.
- (35) Srinivas, G.; Klein, M. L. Coarse-Grain Molecular Dynamics Simulations of Diblock Copolymer Surfactants Interacting with a Lipid Bilayer. *Mol. Phys.* **2004**, *102*, 883–889.
- (36) Kim, M.; Heinrich, F.; Haugstad, G.; Yu, G.; Yuan, G.; Satija, S. K.; Zhang, W.; Seo, H. S.; Metzger, J. M.; Azarin, S. M.; Lodge, T. P.; Hackel, B. J.; Bates, F. S. Spatial Distribution of PEO-PPO-PEO Block Copolymer and PEO Homopolymer in Lipid Bilayers. *Langmuir* **2020**, *36*, 3393–3403.
- (37) Gautier, R.; Bacle, A.; Tiberti, M. L.; Fuchs, P. F.; Vanni, S.; Antonny, B. PackMem: A Versatile Tool to Compute and Visualize Interfacial Packing Defects in Lipid Bilayers. *Biophys. J.* **2018**, *115*, 436–444.
- (38) Cui, H.; Lyman, E.; Voth, G. A. Mechanism of Membrane Curvature Sensing by Amphipathic Helix Containing Proteins. *Biophys. J.* **2011**, *100*, 1271–1279.
- (39) Vamparys, L.; Gautier, R.; Vanni, S.; Bennett, W. F. D.; Tieleman, D. P.; Antonny, B.; Etchebest, C.; Fuchs, P. F. J. Conical Lipids in Flat Bilayers Induce Packing Defects Similar to That Induced by Positive Curvature. *Biophys. J.* **2013**, *104*, 585–593.
- (40) Olzyńska, A.; Kulig, W.; Mikkilainen, H.; Czerniak, T.; Jurkiewicz, P.; Cwiklik, L.; Rog, T.; Hof, M.; Jungwirth, P.; Vattulainen, I. Tail-Oxidized Cholesterol Enhances Membrane Permeability for Small Solutes. *Langmuir* **2020**, *36*, 10438–10447.
- (41) Paxton, W. F.; McAninch, P. T.; Achyuthan, K. E.; Shin, S. H. R.; Monteith, H. L. Monitoring and Modulating Ion Traffic in Hybrid Lipid/Polymer Vesicles. *Colloids Surf., B* **2017**, *159*, 268–276.
- (42) Vanni, S.; Vamparys, L.; Gautier, R.; Drin, G.; Etchebest, C.; Fuchs, P. F. J.; Antonny, B. Amphipathic Lipid Packing Sensor Motifs: Probing Bilayer Defects with Hydrophobic Residues. *Biophys. J.* **2013**, *104*, 575–584.
- (43) Sikdar, S.; Banerjee, M.; Vemparala, S. Effect of Cholesterol on the Membrane Partitioning Dynamics of Hepatitis A Virus-2B Peptide. *Soft Matter* **2021**, *17*, 7963–7977.
- (44) Bennett, W. F. D.; Tieleman, D. P. The Importance of Membrane Defects—Lessons from Simulations. *Acc. Chem. Res.* **2014**, *47*, 2244–2251.
- (45) Ulmschneider, J. P.; Smith, J. C.; White, S. H.; Ulmschneider, M. B. The Importance of the Membrane Interface as the Reference State for Membrane Protein Stability. *Biochim. Biophys. Acta Biomembr.* **2018**, *1860*, 2539–2548.
- (46) Ulmschneider, M. B.; Doux, J. P. F.; Killian, J. A.; Smith, J. C.; Ulmschneider, J. P. Mechanism and Kinetics of Peptide Partitioning into Membranes from All-Atom Simulations of Thermostable Peptides. *J. Am. Chem. Soc.* **2010**, *132*, 3452–3460.
- (47) Gumbart, J. C.; Ulmschneider, M. B.; Hazel, A.; White, S. H.; Ulmschneider, J. P. Computed Free Energies of Peptide Insertion into Bilayers Are Independent of Computational Method. *J. Membr. Biol.* **2018**, *251*, 345–356.
- (48) Vanommeslaeghe, K.; MacKerell, A. D. Automation of the CHARMM General Force Field (CGenFF) I: Bond Perception and Atom Typing. *J. Chem. Inf. Model.* **2012**, *52*, 3144–3154.
- (49) Klauda, J. B.; Venable, R. M.; Freites, J. A.; O'Connor, J. W.; Tobias, D. J.; Mondragon-Ramirez, C.; Vorobyov, I.; MacKerell, A. D.; Pastor, R. W. Update of the CHARMM All-Atom Additive Force Field for Lipids: Validation on Six Lipid Types. *J. Phys. Chem. B* **2010**, *114*, 7830–7843.
- (50) Humphrey, W.; Dalke, A.; Schulten, K. VMD - Visual Molecular Dynamics. *J. Molec. Graphics* **1996**, *14*, 33–38.
- (51) Barden, D. R. *Molecular Dynamics Studies of Biomimetic Membranes*; University of New Hampshire: Durham, 2017.
- (52) Lee, J.; Cheng, X.; Swails, J. M.; Yeom, M. S.; Eastman, P. K.; Lemkul, J. A.; Wei, S.; Buckner, J.; Jeong, J. C.; Qi, Y.; Jo, S.; Pande, V. S.; Case, D. A.; Brooks, C. L.; MacKerell, A. D.; Klauda, J. B.; Im, W. CHARMM-GUI Input Generator for NAMD, GROMACS, AMBER, OpenMM, and CHARMM/OpenMM Simulations Using the CHARMM36 Additive Force Field. *J. Chem. Theory Comput.* **2016**, *12*, 405–413.

- (53) Jo, S.; Kim, T.; Iyer, V. G.; Im, W. CHARMM-GUI: A Web-Based Graphical User Interface for CHARMM. *J. Comput. Chem.* **2008**, *29*, 1859–1865.
- (54) Bekker, H.; Berendsen, H.; Dijkstra, E.; Achterop, S.; van Drunen, R.; van der Spoel, D.; Sijbers, A.; Keegstra, H.; Reitsma, B.; Renardus, M. Gromacs: A Parallel Computer for Molecular Dynamics Simulations. *4th International Conference on Computational Physics (PC 92)*, 1993; Vol. 92, pp 252–256.
- (55) Feller, S. E.; Pastor, R. W. Constant Surface Tension Simulations of Lipid Bilayers: The Sensitivity of Surface Areas and Compressibilities. *J. Chem. Phys.* **1999**, *111*, 1281–1287.
- (56) Wolff, U. Monte Carlo Errors with Less Errors. *Comput. Phys. Commun.* **2004**, *156*, 143–153.
- (57) Flyvbjerg, H.; Petersen, H. G. Error Estimates on Averages of Correlated Data. *J. Chem. Phys.* **1989**, *91*, 461–466.
- (58) Gowers, R.; Linke, M.; Barnoud, J.; Reddy, T.; Melo, M.; Seyler, S.; Domański, J.; Dotson, D.; Buchoux, S.; Kenney, I.; Beckstein, O. M. D. A. MDAnalysis: A Python Package for the Rapid Analysis of Molecular Dynamics Simulations. *Proceedings of the 15th Python in Science Conference*, 2016, Vol. 98, p 105.
- (59) Michaud-Agrawal, N.; Denning, E. J.; Woolf, T. B.; Beckstein, O. M. D. A. MDAnalysis: A toolkit for the analysis of molecular dynamics simulations. *J. Comput. Chem.* **2011**, *32*, 2319–2327.
- (60) Harris, C. R.; Millman, K. J.; van der Walt, S. J.; Gommers, R.; Virtanen, P.; Cournapeau, D.; Wieser, E.; Taylor, J.; Berg, S.; Smith, N. J.; Kern, R.; Picus, M.; Hoyer, S.; van Kerkwijk, M. H.; Brett, M.; Haldane, A.; del Río, J. F.; Wiebe, M.; Peterson, P.; Gérard-Marchant, P.; Sheppard, K.; Reddy, T.; Weckesser, W.; Abbasi, H.; Gohlke, C.; Oliphant, T. E. Array Programming with NumPy. *Nature* **2020**, *585*, 357–362.
- (61) Scherer, M. K.; Trendelkamp-Schroer, B.; Paul, F.; Pérez-Hernández, G.; Hoffmann, M.; Plattner, N.; Wehmeyer, C.; Prinz, J. H.; Noé, F. PyEMMA 2: A Software Package for Estimation, Validation, and Analysis of Markov Models. *J. Chem. Theory Comput.* **2015**, *11*, 5525–5542.
- (62) Jacobs, M. L.; Kamat, N. P. Cell-Free Membrane Protein Expression into Hybrid Lipid/Polymer Vesicles. *Methods Mol. Biol.* **2022**, *2433*, 257–271.

## □ Recommended by ACS

### Passive Macromolecular Translocation Mechanism through Lipid Membranes

Ekaterina Kostyurina, Ralf Biehl, et al.

AUGUST 11, 2022

JOURNAL OF THE AMERICAN CHEMICAL SOCIETY

READ ▶

### Detergent-Free Functionalization of Hybrid Vesicles with Membrane Proteins Using SMALPs

Rosa Catania, Lars J. C. Jeukens, et al.

APRIL 21, 2022

MACROMOLECULES

READ ▶

### Multicomponent Copolymer Planar Membranes with Nanoscale Domain Separation

Maryame Bina, Cornelia G. Palivan, et al.

JUNE 30, 2022

NANO LETTERS

READ ▶

### Improvement of Thermal Stability of Amphipathic Peptide–Phospholipid Nanodiscs via Lateral Association of $\alpha$ -Helices by Disulfide Cross-Linking

Chihiro Anada, Minoru Nakano, et al.

MAY 25, 2022

LANGMUIR

READ ▶

Get More Suggestions >